New Fe–Cr–Mo–Ga–C composites with high compressive strength and large plasticity

K. Werniewicz [a,c,*], U. Kühn [a], N. Mattern [a], B. Bartusch [a], J. Eckert [a], J. Das [a], L. Schultz [a,b], T. Kulik [c]

[a] IFW Dresden, P.O. Box 270116, D-01171 Dresden, Germany
[b] TU Dresden, Institute for Materials Science, D-01062 Dresden, Germany
[c] Warsaw University of Technology, Faculty of Materials Science and Engineering, ul. Wołoska 141, 02-507 Warsaw, Poland

Abstract

A novel nanostructured Fe–Cr–Mo–Ga–C composite derived from a bulk metallic glass-forming alloy composition has been prepared with different carbon content to improve the ductility of this high-strength material. Excellent compressive mechanical properties were found for both samples, which essentially consist of soft gallium-enriched dendrites embedded in a hard chromium- and molybdenum-enriched matrix. The coexistence of the soft and hard phases leads to a composite material with a high fracture strength combined with large ductility. The obtained values of true strength and true strain are 2.9 GPa and 36% for the alloy with lower carbon content and 3.0 GPa and 16% for the alloy with higher carbon content, respectively. It is worth noting that such excellent compressive behavior has never been observed before for any crystalline or glassy structured material.
© 2007 Acta Materialia Inc. Published by Elsevier Ltd. All rights reserved.

1. Introduction

Owing to the rapidity of technological progress, novel materials with unique physical and chemical properties are constantly required. One of civilization's most important and highly developed engineering materials is steel, because the basic element iron is cheap and readily available, and its properties are widely variable by alloying and annealing. In contrast, metallic glasses are a novel class of metallic alloys. Their discovery in 1960 by Duwez et al. opened a new chapter in the history of materials science [1]. Metallic glasses are characterized by high yield and fracture strength, large elasticity [2–4] and improved corrosion resistance compared with their crystalline counterparts [5,6], as well as good magnetic properties in the case of

iron- and cobalt-based glasses [7–9]. Consequently, these materials are currently the subjects of intense research.

This paper reports about investigations on the mechanical behavior of two advanced multi-component iron-based alloys. Since the first synthesis of an iron-based bulk metallic glass (BMG) in 1995 [10], a variety of new iron-based glassy alloys have been developed [11–16]. It was found that these materials exhibit outstanding mechanical properties, which can be exploited for future structural and functional applications [17,18]. Compared with other glass-forming systems, e.g. zirconium- and titanium-based compositions, iron-based glassy alloys show significant higher fracture strength. It has been reported that the strength values for iron-based BMGs are in the range of 2.8–4.0 GPa [13–16,18–20], whereas the zirconium- and titanium-based glasses show a lower fracture strength of about 2 GPa [2,21]. However, the most significant disadvantage of the BMGs is their inhomogeneous deformation at temperatures below the glass transition temperature, with the

negative consequence of a lack of macroscopic plasticity and strain hardening. Thus, if the operating stress exceeds the elastic limit, the materials fail without appreciable strain [2]. Exceptions to this behavior have recently been found for several Cu–Zr–(Ti, Al) glassy alloys, which show room temperature compressive ductility [22,23]. To improve the ductility of the BMGs, novel in situ cast composite materials were developed by modifying the compositions of zirconium-, titanium- and copper-based glassy alloys [24–29]. With this approach, noticeable enhanced plasticity has been achieved for these alloy systems. However, such composite formation has not been reported for iron-based alloys so far. Consequently, the aim of this work was to improve the ductility of the iron-based glass-forming alloys.

The multi-component $Fe_{65.5}Cr_4Mo_4Ga_4P_{12}C_5B_{5.5}$ glassy alloy was chosen as the starting material. This glassy alloy is well known for its good soft magnetic properties and excellent mechanical strength, which have been extensively studied in the past few years [20,30,31]. It exhibits a high fracture strength of 2.8 GPa, but shows almost no plasticity upon compression testing. Based on these results, the main effort has been devoted to improving the ductility of the investigated iron-based alloys. Here, we report on the phase formation and the resulting mechanical properties of two $(Fe_{84.4}Cr_{5.2}Mo_{5.2}Ga_{5.2})_{100-x}C_x$ alloys, with $x = 9$ and 17. The compositions are derived from the $Fe_{65.5}Cr_4Mo_4Ga_4P_{12}C_5B_{5.5}$ BMG by substitution of the elements phosphorus and boron to verify the capability of plastic deformation in the alloy system. Additionally, the influence of carbon on the deformation mode was studied. It must be mentioned that the glass-forming ability of such alloys is not sufficient to obtain a glass structure as a result of the casting process. Nevertheless, excellent mechanical properties were obtained for these materials.

2. Experimental procedure

To achieve compositional homogeneity, alloy A $(Fe_{84.4}Cr_{5.2}Mo_{5.2}Ga_{5.2})_{91}C_9$ and alloy B $(Fe_{84.4}Cr_{5.2}Mo_{5.2}Ga_{5.2})_{83}C_{17}$ were fabricated in the following steps: master alloys with nominal composition of $Fe_{84.4}Cr_{5.2}Mo_{5.2}Ga_{5.2}$ were prepared by arc-melting high-purity elements under a titanium-gettered argon atmosphere. As-prepared ingots were subsequently crushed into pieces and remelted together with an appropriate portion of carbon (9 and 17 at.%) in an induction-casting device. The oxygen contamination level of the master alloys as well as the carbon content were evaluated by hot carrier gas extraction in a helium atmosphere using a LECO TC436DR and in a reactive oxygen atmosphere using a LECO CS444, respectively. The oxygen concentration was determined to be 0.03 at.% The measured values for the carbon content are 9.0 at.% for alloy A and 15.8 at.% for alloy B. These compositions are consistent with the given nominal compositions of alloys A and B. Rod-shaped samples with a length of

70 mm and a diameter of 3 mm were produced by the centrifugal casting technique.

The microstructure of as-cast and deformed samples was examined by X-ray diffraction (XRD) with Co Kα radiation ($\lambda = 0.17889$ nm). The evaluation of the as-prepared state of the samples was continued by scanning electron microscopy (SEM) coupled with wavelength-dispersive X-ray spectroscopy (WDX), using a PHILIPS XL30 microscope equipped with MICROSPEC WDX. Transmission electron microscopy (TEM) investigations and energy-dispersive X-ray spectroscopy (EDX) microanalysis were performed using a JEOL 2000 FX analytical microscope with 200 kV acceleration voltage and an EDAX energy-dispersive X-ray spectrometer. Thin slices from the 3 mm ∅ cast rods were used for preparing the TEM specimens, which were ground, mechanically dimpled and polished by argon ion milling as the final thinning process using a GATAN precision ion-polishing system (PIPS).

The room temperature compression tests and the Vickers hardness tests were performed to study the mechanical behavior. Mechanical tests were carried out using an electromechanical Instron 8562 testing device at a strain rate of 10^{-4} s^{-1}. For the compression tests cylindrical specimens with dimensions of 3 mm diameter × 6 mm length were used. To avoid effects of friction between the specimen and the punches, the contact surfaces of the samples were ground and polished. The samples were deformed until fracture occurred. Furthermore, hardness measurements of particular phases as well as of the whole alloys were done using a Struers Duramin 5 hardness tester. The tests were realized using a typical diamond indenter in the shape of a pyramid. A load of 4.9 N was applied for 10 s. At least 10 indents were performed for each phase to obtain an accurate result.

3. Results and discussion

Fig. 1a and b presents the XRD patterns for the as-cast alloys (black curves) A $(Fe_{84.4}Cr_{5.2}Mo_{5.2}Ga_{5.2})_{91}C_9$ and B $(Fe_{84.4}Cr_{5.2}Mo_{5.2}Ga_{5.2})_{83}C_{17}$. These results clearly indicate that both samples consist of a complex crystalline structure. The microstructure of alloy A is mainly composed of a face-centered cubic (fcc) austenitic phase (γ-Fe) and a body-centered tetragonal (bct) martensitic phase. Besides the reflections of the austenite and martensite, weak additional peaks corresponding to a hexagonal (hP3) [32] chromium/molybdenum carbide $(Cr,Mo)_2C$ are present. Based on the XRD patterns, the volume fraction of the phases was calculated by a multi-phase Rietveld analysis [33], assuming identical chemical composition of the individual structures. This analysis is 41 vol.% austenitic, 42 vol.% martensitic and 17 vol.% hexagonal carbide phase, respectively. Also, for sample B the position of the maxima of the main XRD peaks can be assigned to an fcc austenitic γ-Fe phase. In contrast to alloy A, further reflections indicate the formation of Fe_3C (cementite), with an orthorhombic crystal structure [32]. There is no indication of any other
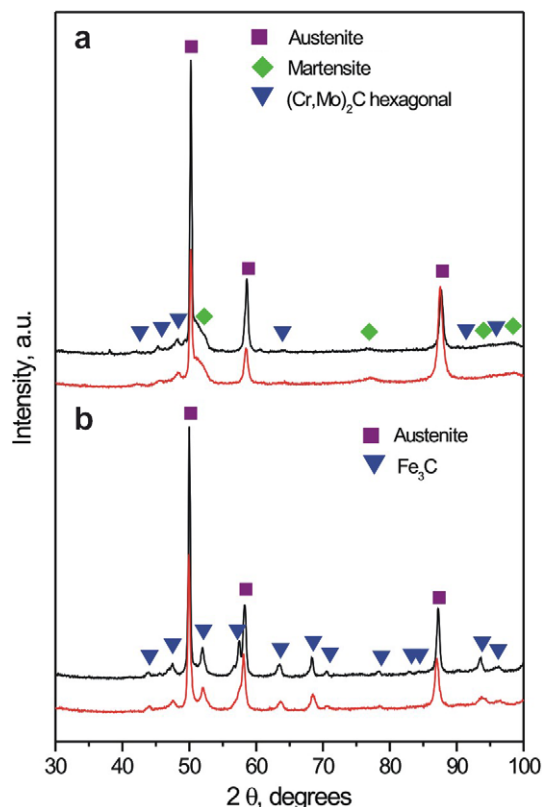
Fig. 1. XRD patterns of the as-cast (black curves) and deformed (red curves) cylindrical rods of the $(Fe_{84.4}Cr_{5.2}Mo_{5.2}Ga_{5.2})_{100-x}C_x$ alloys with (a) $x = 9$ (alloy A) and (b) $x = 17$ (alloy B). (For interpretation of the references to colour in this figure legend, the reader is referred to the web version of this article.)

phases in this alloy. Volume fractions of 25 vol.% Fe_3C and 75 vol.% fcc γ-Fe were estimated from the Rietveld analysis.

The SEM images (Fig. 2a and b) illustrate the spatial distribution, the morphology, the size, and the volume fraction of the phases in the center area of as-cast samples A and B. Alloy A presents three fine-dispersed phases, whereas the two main phases exhibit grain sizes of about 5 μm. The martensitic phase rather shows an elongated shape. The microstructure of alloy B presents only two phases, with clearly different volume fractions. The fcc γ-Fe phase (dark phase) is more spherical and the grain size is slightly bigger compared with alloy A. The outer regions of both specimens (not shown here) reveal a finer microstructure. It is well known that the first contact of the melt with the copper wall of the mold leads to higher cooling rates during solidification compared with the inner part [34]. Therefore, the grain size of the phases in the center region of the cylinders is slightly bigger.

The SEM images (Fig. 2c and d) display the microstructure of specimens A and B in more detail. Alloy A shows a complex microstructure consisting of micrometer-sized dendrites of the austenitic phase, large plates of martensite and small precipitates (black phase) at the boundaries of the martensitic phase, which can be assigned to (Cr,Mo)-carbides. Electron diffraction patterns (not shown here) obtained from the two main phases (austenite and martensite) support the fcc and bct structure, respectively. The EDX results (summarized in Table 1) reveal that the dendritic phase is enriched in iron and gallium compared with
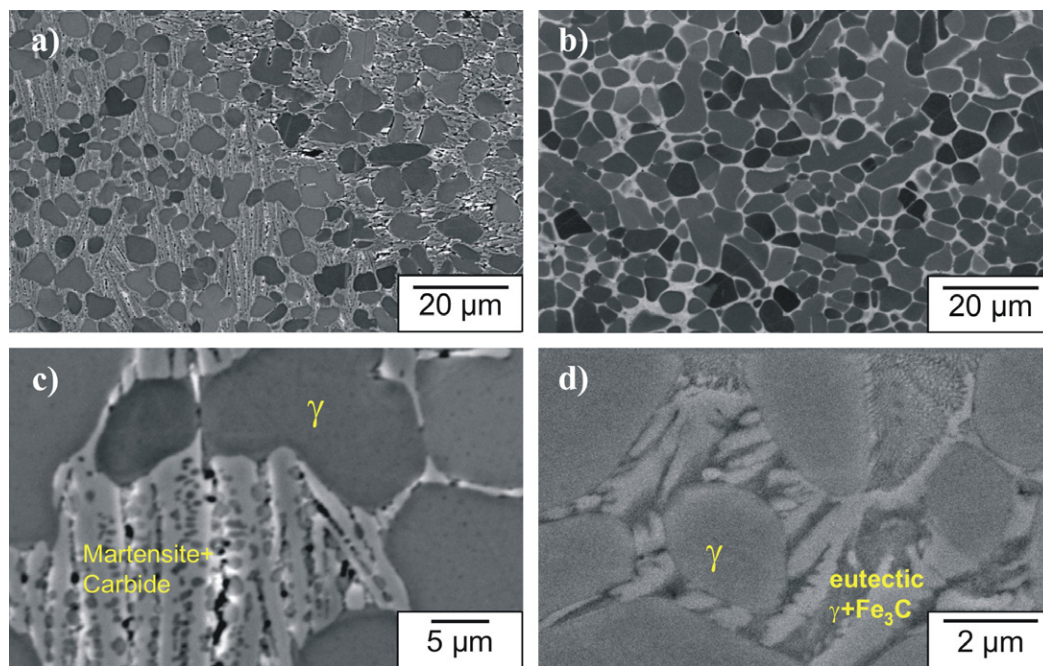

Fig. 2. SEM images of as-cast alloys $(Fe_{84.4}Cr_{5.2}Mo_{5.2}Ga_{5.2})_{91}C_9$ (a, c) and $(Fe_{84.4}Cr_{5.2}Mo_{5.2}Ga_{5.2})_{83}C_{17}$ (b, d). The SEM (BSE mode) images (a, b) show the homogeneous distribution, the size and the morphology of the fcc γ-Fe phase (dark gray phase). The SEM images (c, d) reveal the interdendritic phases: (c) (BSE-mode) the martensitic phase with M_2C carbides; and (d) (SE-mode) the interdendritic eutectic phases, γ-Fe and Fe_3C.

Table 1
EDX analysis of the different phases compared with the nominal composition of the alloy A and B

|	Alloying components, at.%				
	Fe	Cr	Mo	Ga	C
Nominal composition: alloy (A)	**76.9**	**4.7**	**4.7**	**4.7**	**9**
γ-Austenite	78.6	3.3	4.0	8.6	5.5
Martensite	77.7	8.6	6.6	1.6	5.5
Carbide (Cr,Mo)$_2$C	47.6	9.8	16.8	1.8	24.0
Nominal composition: alloy (B)	**70.1**	**4.3**	**4.3**	**4.3**	**17**
γ-Austenite	82.5	2.6	3.1	7.2	4.6
Cementite Fe(Cr,Mo)$_3$C	54.8	7.1	7.9	0.1	30.1

Fig. 3. Schematic illustration of the phase transformation steps at specific temperatures (liquidus temperature T_l, solidus temperature T_s, starting temperature of martensitic transformation M_s) of the alloy A, $(Fe_{84.4}Cr_{5.2}Mo_{5.2}Ga_{5.2})_{91}C_9$, during copper mould casting.

the nominal composition. The dendritic phase is a γ-Fe(C,Ga) solid solution, whereas carbon stabilizes the fcc structure of iron [35]. Both interdendritic phases (the martensitic phase and the carbides) show significantly higher chromium and molybdenum concentrations in comparison with the nominal alloy composition.

The three phases present in alloy A (austenite, martensite, carbides) are the typical phases existing in steels. Therefore, to consider the solidification behavior of alloy A, the iron–carbon phase diagram and the non-equilibrium diffusionless transformation mechanism of martensite were used as a tool to try to understand the phase formation of alloy A [35]. However, such a phase configuration (round-shaped austenite in coexistence with martensite and relatively high amounts of carbides already in the non-tempered state) is atypical for steels. Usually, lath or plate martensite transforms from the parent austenite and, in the case of incomplete martensitic transformation, residual austenite is retained between the laths or plates of martensite [36]. Furthermore, the formation of carbides in chromium- and molybdenum-containing steels is generally induced by tempering at 500–700 °C, i.e. they do not form during solidification [37].

Fig. 3 shows schematically the potential stepwise phase formation during the solidification of alloy A. Attention should be paid to the fact that the primary formed austenite shows a composition that is significantly different from the parent austenite, which shears into martensite by an athermal transformation process [36]. The first phase, which precipitates from the melt, is an fcc phase with low carbon content, i.e. the remaining melt will be continuously enriched in carbon. Gallium, chromium and molybdenum are substitutional alloying elements to iron [35], but only gallium is completely dissolved in the primary γ-solid solution, despite the fact that it has the lowest melting point of the alloying elements. This behavior is because chromium and molybdenum are very strong carbide-forming elements [36], whereas gallium obviously does not form phases with carbon (a gallium–carbon phase diagram is not available). One can assume that the formation of the γ-Fe(C,Ga) solid solution occurs simultaneously to the carbide formation. (Cr,Mo)$_2$C with hexagonal structure was mainly found at the grain boundaries of the martensite. The strong affinity
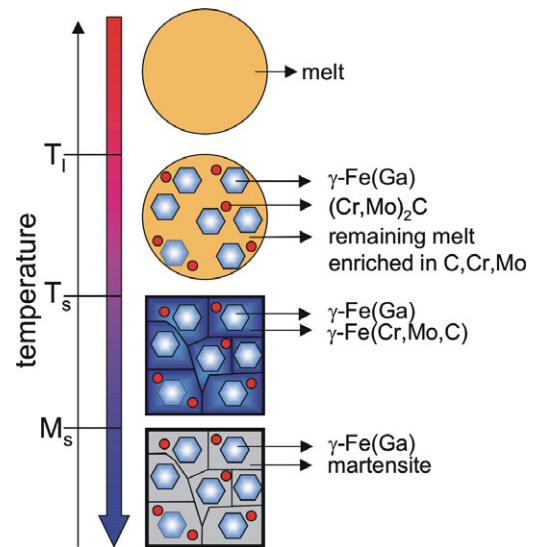
between chromium–carbon and molybdenum–carbon is certainly the reason why only the interdendritic phases (martensite and carbides) contain these elements in higher concentrations.

With progressing solidification the γ-Fe solid solution becomes more and more enriched in chromium and molybdenum besides the carbide formation. Thus, on cooling from temperatures where the austenite is no longer stable and because chromium and molybdenum tend to stabilize the body-centered cubic structure of iron, the fraction of the austenite that is locally enriched in chromium and molybdenum must transform into another phase. A diffusion-controlled mechanism is suppressed by the rapid cooling. Therefore, these parts of the austenite transform into martensite, which is supersaturated in carbon.

The detailed microstructure of alloy B is presented in the SEM image in Fig. 2d. The micrograph reveals two phases: a dendritic phase, which is assigned to the austenite, and interdendritic eutectic phases of austenite and cementite. These are the typical phases of cast iron [36]. The formation of cementite is, in contrast to the martensite formation, diffusion-controlled and accompanied by a rearrangement of the iron atoms from the fcc structure to the orthorhombic structure of the cementite [36]. Similar to the observations made for alloy A, the austenitic phase is enriched in iron and gallium and depleted in chromium, molybdenum and carbon in comparison with the nominal alloy composition. The last three elements are found in much higher concentrations in the (Fe,Cr,Mo)$_3$C phase (cementite). The solidification behavior and, therefore, the microstructure of alloy B differ from those of alloy A, due to the higher carbon content of alloy B (17 at.%). The composition is near to the eutectic point of the iron–carbon phase diagram, where austenite and cementite show phase equilibrium. Consequently, the alloy solidifies at a
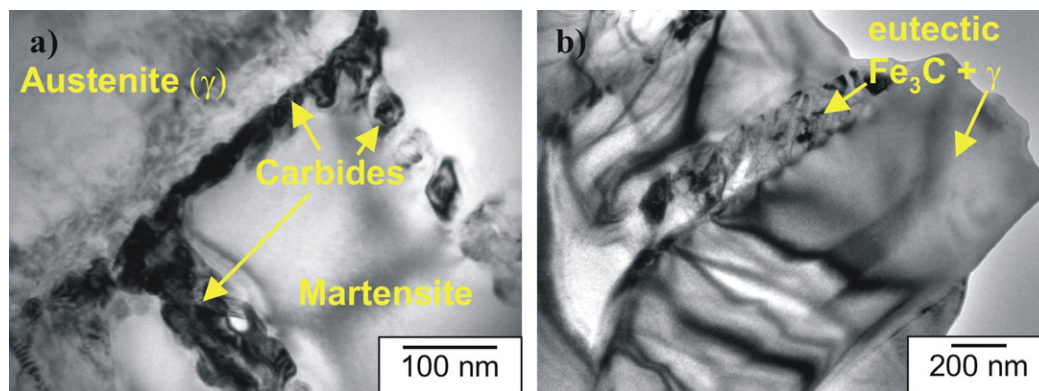
Fig. 4. Bright-field TEM images of as-cast alloys $(Fe_{84.4}Cr_{5.2}Mo_{5.2}Ga_{5.2})_{91}C_9$ (a) and $(Fe_{84.4}Cr_{5.2}Mo_{5.2}Ga_{5.2})_{83}C_{17}$ (b). For both alloys the high distortion of the interdendritic phases is shown, mainly caused by lattice supersaturation with carbon atoms.

lower temperature compared with alloy A and the melting interval (T_1 to T_s) is significantly shorter. Obviously, these characteristics prevent the precipitation of high melting (Cr,Mo)-carbides. Primary austenite (gallium-rich γ-Fe solid solution) nucleates and grows into a dendritic array during the melting interval. When the eutectic concentration is reached, the excess carbon precipitates as the metastable $(Fe,Cr,Mo)_3C$ phase together with γ-Fe by a eutectic reaction.

Bright-field TEM images (Fig. 4a and b) reveal the characteristics of the interdendritic phases of both alloys. For composition A (Fig. 4a), the carbides are bead-shaped and placed at the interfaces of the austenite and martensite. The size of the carbide precipitates is about 20 nm. The formation of the martensite is connected with an increase of volume, due to the trapping of carbon atoms in one set of octahedral interstitial sites of the body-centered structure [36]. Therefore, the martensite is highly distorted and high strain energy is associated with the martensitic structure. Also the interdendritic eutectic phases (austenite + cementite) of composition B reveal significant straining in the TEM image (Fig. 4b) (see the white, grey and black bending lines caused by lattice distortion). The main reason for the distortions is, similar to alloy A, the lattice supersaturation with carbon atoms on interstitial sites.

It is well known that martensite, carbides and cementite are the sources of hardness and high strength in steels, but they are also responsible for the high brittleness of the material [36]. The reasons are manifold, e.g. the special lattice structure, generation of internal stress, solid solution strengthening, particle strengthening. Microhardness measurements of the particular phases and mixed phases, respectively, for alloys A and B were performed to confirm these expectations and to obtain specific values. The average value for the chromium- and molybdenum-rich interdendritic phases (martensite + carbide for alloy A) is 7.3 GPa and for the eutectic phases (austenite + cementite for alloy B) is 5.0 GPa, respectively. Meanwhile, the microhardness of the gallium-rich dendritic austenite was determined to be 3.3 GPa for A and 2.9 GPa for B, respec-

tively. The value of 7.3 GPa (martensite + carbide) is similar to the high microhardness of 8.7 GPa obtained for the glassy $Fe_{65.5}Cr_4Mo_4Ga_4P_{12}C_5B_5$ BMG [20]. The combination of phases with significantly different hardness values clearly indicate that the present alloys can be treated to form composite materials which show both high strength and good ductility.

Room temperature compressive true stress–true strain curves for the as-cast alloys A $(Fe_{84.4}Cr_{5.2}Mo_{5.2}Ga_{5.2})_{91}C_9$ and B $(Fe_{84.4}Cr_{5.2}Mo_{5.2}Ga_{5.2})_{83}C_{17}$ (3 mm diameter cylinders) are presented in Fig. 5 (the engineering stress–strain curves are shown in the inset of Fig. 5). The mechanical properties for both alloys are listed in Table 2. Additionally, the mechanical properties of fully glassy $Fe_{65.5}Cr_4$-$Mo_4Ga_4P_{12}C_5B_{5.5}$ (C) [20] and $[(Fe_{0.5}Co_{0.5})_{0.75}B_{0.2}$-$Si_{0.05}]_{96}Nb_4$ (D) [14] are given for comparison. The most distinctive and remarkable mechanical features are on one hand the large increase in ductility to $\varepsilon_{f(true)} = 36.2\%$ for A and $\varepsilon_{f(true)} = 16.4\%$ for B without any reduction of
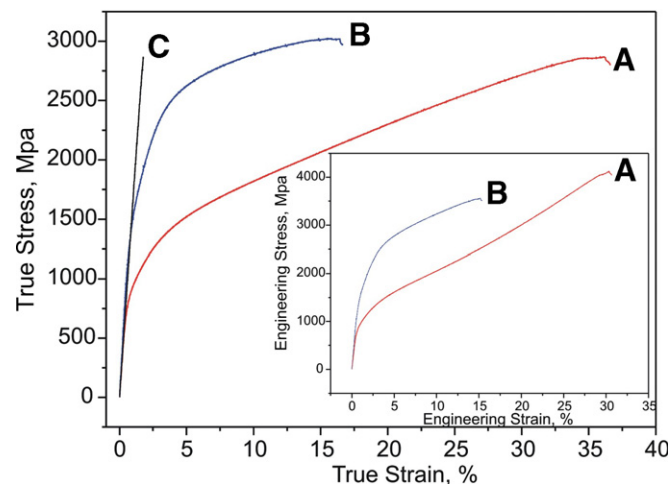

Fig. 5. Room temperature true stress–strain curves of (A) $(Fe_{84.4}Cr_{5.2}$-$Mo_{5.2}Ga_{5.2})_{91}C_9$, (B) $(Fe_{84.4}Cr_{5.2}Mo_{5.2}Ga_{5.2})_{83}C_{17}$ and (C) $Fe_{65.5}Cr_4Mo_4$-$Ga_4P_{12}C_5B_5$ (BMG) under compression, illustrating the strong influence of the microstructure on the mechanical behavior. The inset shows the engineering stress–strain curves of alloys A and B.

Table 2
Engineering and true values of room temperature compression tests for (A) $(Fe_{84.4}Cr_{5.2}Mo_{5.2}Ga_{5.2})_{91}C_9$ and (B) $(Fe_{84.4}Cr_{5.2}Mo_{5.2}Ga_{5.2})_{83}C_{17}$: Young's modulus E, yield stress σ_y, yield strain ε_y, ultimate compression stress σ_{max}, and fracture strain ε_f

Alloy/sample dimensions	Engineering values					True values	
	E (GPa)	σ_y (MPa)	ε_y (%)	σ_{max} (MPa)	ε_f (%)	σ_{max} (MPa)	ε_f (%)
(A)/∅ 3 mm	162	833	0.7	4116	30.4	2868	36.2
(B)/∅ 3 mm	208	1410	0.9	3561	15.2	3026	16.4
(C)/2 × 2 mm² [20]	161	2820	1.8	2840	1.9		
(D)/∅ 2 mm [14]	210	4070	2.0	4210	2.25		

The mechanical properties of $Fe_{65.5}Cr_4Mo_4Ga_4P_{12}C_5B_{5.5}$ (C) and $[(Fe_{0.5}Co_{0.5})_{0.75}B_{0.2}Si_{0.05}]_{96}Nb_4$ (D) BMGs are given for comparison.

the fracture strength compared with the iron-based BMG. The ultimate compression stress of sample B ($\sigma_{max} = 3026$ MPa) is even superior to the corresponding values of monolithic iron-based BMG C ($\sigma_{max} = 2840$ MPa). On the other hand, the yield strength decreases significantly from the BMG C ($\sigma_y = 2820$ MPa) to alloy B ($\sigma_y = 1410$ MPa) and to alloy A ($\sigma_y = 833$ MPa), i.e. the high values obtained for maximum strength for alloys A and B are connected with a pronounced strain hardening behavior. Especially for alloy A there is a large increase in the flow stress of about 2000 MPa (from 833 to 2868 MPa). It is worth mentioning that such a combination of high compressive strength together with large ductility, as obtained for $(Fe_{84.4}Cr_{5.2}Mo_{5.2}Ga_{5.2})_{91}C_9$ A and $(Fe_{84.4}Cr_{5.2}Mo_{5.2}Ga_{5.2})_{83}C_{17}$ B have never been observed before for any crystalline as well as glassy alloys. The unique and outstanding mechanical behavior of alloys A and B, i.e. the very strong work hardening in case of alloy A and the high yield and fracture strength coupled with good ductility of alloy B, are based on strong and effective interactions between the soft and ductile (austenite) and the hard and brittle (martensite, cementite, and carbides) components of the microstructure, where the microstructure includes not only the crystallographic lattice of the present phases but also the content of point defects, dislocation density and spatial distribution, grain and twin boundaries, and extraneous atoms in solution [37].

Considering the fact that the martensitic transformation can also be induced by applied external stress at temperatures above M_s [38], detailed observations on the microstructure of as-deformed samples were done. It was expected that the investigated alloys subjected to compressive deformation would undergo an A → M transformation. In order to verify our assumptions, XRD measurements were carried out. The XRD results obtained for deformed compression test samples A and B (red curves in Fig. 1a and b) clearly reveal a significant increase in defects compared with the as-prepared state as well as texture formation, especially in the austenitic phase. But there is no phase transformation of the austenite into martensite,

which could easily explain the large amount of work hardening. Obviously, the mechanical behavior of the presented alloys is rather governed by conventional deformation mechanisms, such as development of a texture on the one hand and dislocation accumulation and motion as well as obstruction of dislocation movement by grain boundaries, obstacles, etc. on the other hand.

Because of the composite nature of the studied iron-based alloys, variations in the fracture behavior between the particular phases were investigated. It is well known that the presence of a ductile dendritic phase in the microstructure of a composite BMG is beneficial for its plasticity [24–29]. To get more information on the crack distribution appearing upon compression, the microstructures as well as the fracture surfaces of deformed specimens were analyzed by SEM, as shown in Fig. 6a–d. The first two pictures (Fig. 6a and b) reveal a high number of cracks. The cracks propagate mostly through the interdendritic phases (as indicated by small yellow arrows in Fig. 6a and b), whereas the interior of the dendrites remains intact. Additionally, some single cracks proceeding along the γ-Fe phase boundaries are also present (as denoted by large yellow arrows in Fig. 6b).

These observations indicate that the soft dendritic precipitates of the austenitic phase efficiently prevent the propagation of cracks, but the cracks initiated under compressive loading in the investigated A and B samples are confined to the interdendritic regions. The fcc γ-Fe particles act as obstacles that hinder the flow deformation, and hence cause pronounced strain hardening. The described observations have been additionally proved by detailed studies on the fracture surfaces of the iron-based composite materials. The morphology of the fracture surfaces of as-deformed cylindrical rods is presented in Fig. 6c and d. As shown in Fig. 6c, the surface appears to consist of a high number of cracks. Furthermore, vein patterns as well as void-like "black dimples" are visible (marked by red and blue arrows in Fig. 6c).

According to the previously described observations, the absence of the cracks inside the dendritic phase was corroborated (as presented in Fig. 6d). The appearance of the above-mentioned features on the fracture surfaces of the examined alloys clearly indicates that the materials have experienced large deformation before final failure. Based on the analyses carried out, it is evident that the combination of the hard interdendritic phases (martensite, cementite, carbide) with the ductile dendritic precipitates (austenite) leads to a high strength from the matrix connected with very good plasticity from the dendrites. Considering the differences in the microstructures of samples A and B, the detailed clarification of the applied mechanisms of the strengthening is given below.

Although alloy A contains a lower volume fraction of the ductile fcc austenitic phase (41 vol.%) in comparison with alloy B (75 vol.% fcc), the achieved plasticity is with $\varepsilon_f = 36.2\%$, which is significantly higher than that of alloy B ($\varepsilon_f = 16.4\%$). The high amount of martensite as well as
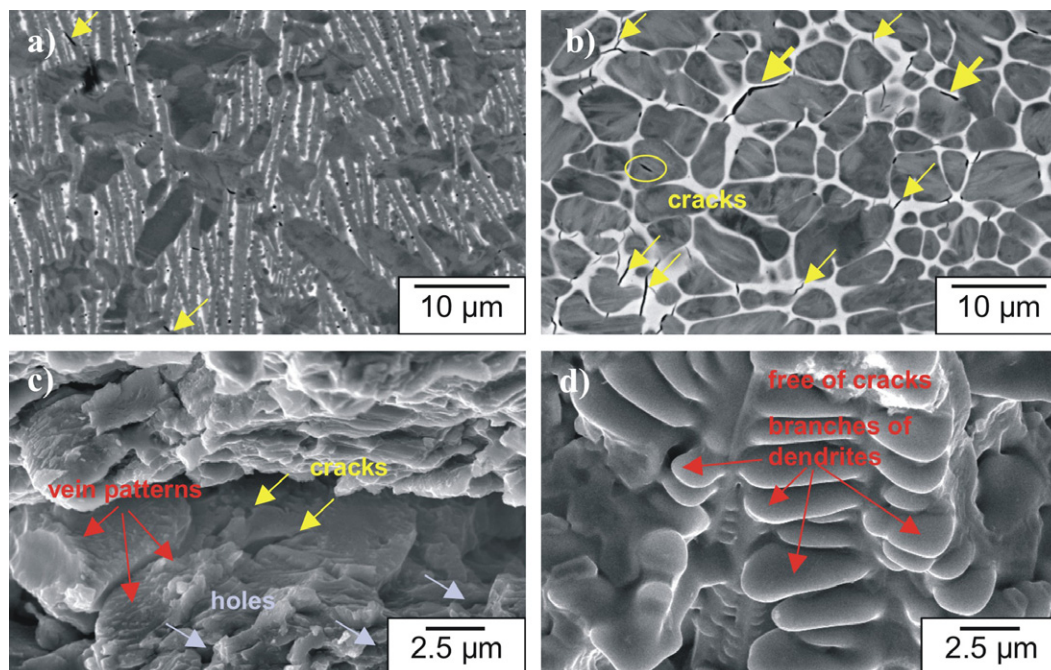
Fig. 6. Observations on deformed cross-section and fracture surface. SEM backscattered electron images of the cross-section (a, b) and SEM secondary electron images of the fracture surface (c, d) of alloys $(Fe_{84.4}Cr_{5.2}Mo_{5.2}Ga_{5.2})_{91}C_9$ (a, c) and $(Fe_{84.4}Cr_{5.2}Mo_{5.2}Ga_{5.2})_{83}C_{17}$ (b, d). (b) The propagation paths of the cracks formed under compressive load. Deformation proceeds along the interdendritic phase either in an intergranular manner (small yellow arrows) or in a transgranular manner (large yellow arrows). Only the single crack cutting through the ductile dendritic phase was recognized (as denoted by yellow circle). Obviously, crack propagation is obstructed by dendrites. (c, d) The fracture features for samples A and B. The occurrence of the well-developed vein patterns, as well as cracks and holes on the fracture morphology, was observed. The presence of the vein pattern indicates that the material has experienced large deformation before failure. A higher magnification picture of the interior of the dendrite (d) confirmed the absence of cracks inside the fcc γ-Fe dendritic phase. (For interpretation of the references to colour in this figure legend, the reader is referred to the web version of this article.)

the carbides in the microstructure of A does not lead to a material with a high yield strength. Furthermore, the Young's modulus for alloy A is relatively low ($E = 162$ GPa). The advantage of this alloy is its good work hardening ability, which is typically caused by enhancing the intensity of the elastic interaction of dislocations by increasing their density under an applied stress. The large strengthening effect can be assigned mainly to a variety of mechanisms that stop dislocation glide. The small carbides act as strong obstacles just like the solute atoms in the crystal lattices and the grain/phase boundaries.

The high yield and true fracture strength ($\sigma_y = 1410$ MPa, $\sigma_f = 3026$ MPa) of alloy B are clearly a consequence of the hard cementite, because the solute strengthening effect of the second existing phase, the fcc phase, is rather small [37]. Presumably the grain boundaries of the austenitic fcc phase hinder dislocation glide, leading to the development of significant strain gradients in the material. The cementite (Fe_3C), which additionally contains chromium and molybdenum, contributes hardness and brittleness to the material because of the asymmetrical orthorhombic lattice structure, which is characterized by a low number of slip systems [34]. In contrast, the fcc phase is ductile. Therefore, the mechanical response of such a composite structure leads to high strength in combination with considerable plastic deformation.

4. Conclusions

Crystalline rod-shaped samples with nominal compositions $(Fe_{84.4}Cr_{5.2}Mo_{5.2}Ga_{5.2})_{91}C_9$ (alloy A) and $(Fe_{84.4}Cr_{5.2}Mo_{5.2}Ga_{5.2})_{83}C_{17}$ (alloy B) were prepared by centrifugal casting. The relationship between the chemical composition, the microstructure and the mechanical behavior was demonstrated. The two variations of carbon content (9 and 17 at.%) result in significant changes in the deformation mode. With increasing carbon concentration, the ductility of the investigated alloys decreases from $\varepsilon_f = 36\%$ to $\varepsilon_f = 16\%$. In strong contrast, the apparent fracture strength is nearly the same, i.e. $\sigma_f = 2.9$ GPa for alloy A and $\sigma_f = 3.0$ GPa for alloy B, respectively. While the obtained values of fracture strength are similar to data reported by Stoica et al. for $Fe_{65.5}Cr_4Mo_4Ga_4P_{12}C_5B_5$ BMG ($\sigma_f = 2.8$ GPa), the values of fracture strain are greatly improved for the crystalline alloys.

The structural observations performed for alloys A and B reveal the coexistence of a ductile gallium-enriched dendritic phase in combination with high strength chromium- and molybdenum-enriched interdendritic phase(s). Therefore, the resulting mechanical behavior can be explained as being due to the formation of a composite material with a specific complex crystalline structure. The combination of ductile and high strength precipitates is responsible for the excellent mechanical properties. Based on these findings,

this type of novel high strength and ductile material shows great promise for the further development of iron-based alloys as engineering materials.

Acknowledgements

References

[1] Klement W, Willens RH, Duwez P. Nature 1960;187:869.
[2] Inoue A, Zhang T, Masumoto T. Mater Trans JIM 1995;36:391.
[3] Wang X, Yoshii I, Inoue A, Kim Y-H, Kim I-B. Mater Trans JIM 1999;40:1130.
[4] Leonhard A, Heilmaier M, Eckert J, Schultz L. Mater Res Soc Symp Proc 1999;554:137.
[5] Masumoto T, Hashimoto K. Ann Rev Mater Sci 1978;8:215.
[6] Gebert A, Mummert K, Eckert J, Schultz L, Inoue A. Mater Corr 1997;48:293.
[7] Yoshizawa Y, Oguma S, Yamauchi K. J Appl Phys 1988;64:6044.
[8] Inoue A, Shen BL, Koshiba H, Kato H, Yavari AR. Acta Mater 2004;52:1631.
[9] Schlorke N, Eckert J, Schultz L. J Phys D 1999;32:855.
[10] Inoue A, Gook JS. Mater Trans JIM 1995;36:1180.
[11] Inoue A, Zhang T, Takeuchi A. Appl Phys Lett 1997;71:464.
[12] Ponnambalam V, Poon SJ, Shiflet GJ, Keppens VM, Taylor R, Petculescu G. Appl Phys Lett 2003;83:1131.
[13] Ponnambalam V, Poon SJ, Shiflet GJ. J Mater Res 2004;19:1320.
[14] Inoue A, Shen BL, Chang CT. Acta Mater 2004;52:4093.
[15] Lu ZP, Liu CT, Thompson JR, Porter WD. Phys Rev Lett 2004;92:245503.
[16] Shen BL, Inoue A. J Mater Res 2005;20:1.
[17] Greer AL. Science 1995;267:1947.
[18] Salimon AI, Ashby MF, Bréchet Y, Greer AL. Mater Sci Eng 2004;A375–377:385–8.
[19] Inoue A, Shen BL, Yavari AR, Greer AL. J Mater Res 2003;18:487.
[20] Stoica M, Eckert J, Roth S, Zhang ZF, Schultz L, Wang WH. Intermetallics 2005;13:764.
[21] Zhang T, Inoue A. Mater Trans JIM 1998;39:857.
[22] Das J, Tang MB, Kim KB, Theissmann R, Baier F, Wang WH, et al. Phys Rev Lett 2005;94:205501-1.
[23] Lee S-W, Huh M-Y, Fleury E, Lee J-C. Acta Mater 2006;54:349.
[24] Hays CC, Kim CP, Johnson WL. Phys Rev Lett 2000;84:2901.
[25] Kühn U, Eckert J, Mattern N, Schultz L. Appl Phys Lett 2002;80:2478.
[26] He G, Eckert J, Löser W, Schultz L. Nat Mater 2003;2:33.
[27] Louzguine DV, Kato H, Inoue A. Appl Phys Lett 2004;84:1088.
[28] Eckert J, Das J, Kim KB, Baier F, Tang MB, Wang WH, et al. Intermetallics 2006;14:876.
[29] Kim KB, Das J, Baier F, Tang MB, Wang WH, Eckert J. Appl Phys Lett 2006;88:051911.
[30] Stoica M, Eckert J, Roth S, Schultz L, Yavari AR, Kvick A. J Metastab Nanocryst Mater 2002;12:77.
[31] Stoica M, Degmova J, Roth S, Eckert J, Grahl H, Schultz L, et al. Mater Trans JIM 2002;43:1966.
[32] Villars P, Calvert LD. Pearson's Handbook of Crystallographic Data for Intermetallic Phases, vol. 2. Materials Park (OH): ASM International; 1991. p. 877.
[33] Young RA. The Rietveld Method. Oxford: Oxford University Press/International Union of Crystallography; 1993. p. 1–298.
[34] Gottstein G. Physikalische Grundlagen der Materialkunde. Berlin: Springer; 1998.
[35] Massalski TB, Okamoto H, Subramanian PR, Kacprzak L. Binary Alloy Phase Diagrams. Materials Park (OH): ASM International; 1990. p. 837–1726.
[36] Cahn RW, Haasen P, Kramer EJ. Constitution and properties of steels. Materials Science and Technology, vol. 7. Weinheim: Wiley-VCH Verlag; 2005. p. 3–736.
[37] Cahn RW, Haasen P, Kramer EJ. Plastic deformation and fracture of materials. Materials Science and Technology, vol. 6. Weinheim: Wiley-VCH Verlag; 2005. p. 3–629.
[38] Cahn RW, Haasen P, Kramer EJ. Phase transformation in materials. Materials Science and Technology, vol. 5. Weinheim: Wiley-VCH Verlag; 2005. p. 368–87.